

Cite this: *J. Mater. Chem. A*, 2021, 9, 16137

# Enhancing interfacial charge transfer in a WO<sub>3</sub>/BiVO<sub>4</sub> photoanode heterojunction through gallium and tungsten co-doping and a sulfur modified Bi<sub>2</sub>O<sub>3</sub> interfacial layer†

Umesh Prasad,<sup>a,b</sup> James L. Young,<sup>\*b</sup> Justin C. Johnson,<sup>b</sup> Deborah L. McGott,<sup>b,c</sup> Hengfei Gu,<sup>d</sup> Eric Garfunkel<sup>d</sup> and Arunachala M. Kannan<sup>b,\*a</sup>

Photoanodes containing a WO<sub>3</sub>/BiVO<sub>4</sub> heterojunction have demonstrated promising photoelectrochemical water splitting performance, but the ability to effectively passivate the WO<sub>3</sub>/BiVO<sub>4</sub> interface has limited charge transport and collection. Here, the WO<sub>3</sub>/BiVO<sub>4</sub> interface is passivated with a sulfur-modified Bi<sub>2</sub>O<sub>3</sub> interfacial layer with a staggered band edge alignment to facilitate charge transfer and lifetime. Additionally, BiVO<sub>4</sub> was co-doped with Ga<sup>3+</sup> at Bi<sup>3+</sup> sites and W<sup>6+</sup> at V<sup>5+</sup> sites (*i.e.*, (Ga,W):BiVO<sub>4</sub>) to improve the light absorption and photogenerated charge carrier concentration. The optimized WO<sub>3</sub>/S:Bi<sub>2</sub>O<sub>3</sub>/(Ga,W):BiVO<sub>4</sub> photoanode exhibited a photocurrent density of 4.0 ± 0.2 mA cm<sup>-2</sup> compared to WO<sub>3</sub>/(Ga,W):BiVO<sub>4</sub> with 2.8 ± 0.12 mA cm<sup>-2</sup> at 1.23 V<sub>RHE</sub> in K<sub>2</sub>HPO<sub>4</sub> under simulated AM 1.5G illumination. Time-resolved photoluminescence spectroscopic analysis of the WO<sub>3</sub>/S:Bi<sub>2</sub>O<sub>3</sub>/(Ga,W):BiVO<sub>4</sub> electrode validated the enhanced interfacial charge transfer kinetics. In *operando* femto- and nano-second transient absorption spectroscopy confirmed the presence of long-lived photogenerated charge carriers and revealed lower recombination initially due to rapid charge separation of WO<sub>3</sub>/S:Bi<sub>2</sub>O<sub>3</sub>/(Ga,W):BiVO<sub>4</sub>. The distribution and role of sulfur was further investigated using EDAX, XPS and TOF-SIMS depth profiling. Finally, a Co-Pi co-catalyst layer was added to achieve a photocurrent of 5.1 ± 0.25 mA cm<sup>-2</sup> and corresponding H<sub>2</sub> generation rate of 67.3 μmol h<sup>-1</sup> cm<sup>-2</sup> for the WO<sub>3</sub>/S:Bi<sub>2</sub>O<sub>3</sub>/(Ga,W):BiVO<sub>4</sub>/Co-Pi photoanode.

Received 5th May 2021  
Accepted 27th June 2021

DOI: 10.1039/d1ta03786b

rsc.li/materials-a

## 1. Introduction

Hydrogen generation by solar assisted photocatalytic water splitting is an attractive route to store solar energy in the form of chemical fuels.<sup>1–3</sup> For such an application, efficient photon harvesting semiconducting oxides have been studied extensively due to their superior electrochemical stability, low cost and natural abundance.<sup>3</sup> Monoclinic n-type bismuth vanadate

(BiVO<sub>4</sub>) is a promising semiconductor material for the oxygen evolution reaction (OER).<sup>4</sup> It possesses a bandgap of ~2.4 eV, conduction band (CB) edge close to 0 volt *vs.* the reversible hydrogen electrode (V<sub>RHE</sub>) and deep valence band (VB) position (~2.4 V<sub>RHE</sub>) that generates a substantial thermodynamic driving force for oxygen evolution.<sup>5,6</sup> The effective defect-tolerant nature<sup>5</sup> with moderate charge transport properties facilitates BiVO<sub>4</sub> to achieve a theoretical photocurrent density (PCD) of up to ~7.5 mA cm<sup>-2</sup> at 1.23 V<sub>RHE</sub> under simulated AM 1.5G illumination (100 mW cm<sup>-2</sup>). However, OER properties of BiVO<sub>4</sub> suffer from low charge transfer rates due to excessive surface recombination on the ps–ns time scale.<sup>7,8</sup> In parallel, the desirable water oxidation occurs at a slower time scale, typically over the ms–s range, due its four-electron reaction mechanism.<sup>6,7,9</sup> Fast charge separation and transport of photo-generated electron–hole pairs are essential for efficient water oxidation.<sup>8,10</sup> Several strategies have been employed to enhance the charge separation and transfer such as composition tuning or doping,<sup>5,10</sup> and formation of homo- and hetero-junctions,<sup>5,11,12</sup> passivation layer<sup>13</sup> and co-catalyst.<sup>14</sup> Tungsten (W) and molybdenum (Mo) have been extensively studied as donor-type dopants in BiVO<sub>4</sub> to increase the charge carrier density,

<sup>a</sup>The Polytechnic School, Ira A. Fulton Schools of Engineering, Arizona State University, Mesa, AZ 85212, USA. E-mail: amk@asu.edu

<sup>b</sup>National Renewable Energy Laboratory, Golden, CO 80401, USA. E-mail: james.young@nrel.gov

<sup>c</sup>Colorado School of Mines, Golden, CO 80401, USA

<sup>d</sup>Department of Chemistry and Chemical Biology, Rutgers University, Piscataway, NJ 08854, USA

† Electronic supplementary information (ESI) available: Additional information including photoelectrochemical, Mott–Schottky, and UV-vis measurements, separation and transfer efficiency calculations, SEM, XRD, XPS, TOF-SIMS, and the Randle circuit. Details of the calculation process of theoretical photocurrent, charge transport, IPCE, APCE, integrated current, absorption efficiency evaluation. Tables including data summary, TRPL, TAS and comparison of improved photocurrent density in the WO<sub>3</sub>/BiVO<sub>4</sub> heterojunction with an additional layer. See DOI: 10.1039/d1ta03786b

mobility and minimize recombination pathways at solid/solid and solid/electrolyte interfaces.<sup>11,15</sup> Along with composition tuning, formation of heterojunctions, particularly, type-II heterojunction formation between  $\text{WO}_3$  (bandgap: 2.7 eV, VB: 0.4 eV & CB: 3.1 eV) and  $\text{BiVO}_4$  (VB: 0.02 eV & CB: 2.4 eV) is efficient due to appropriate band alignment, which promotes spatial charge separation and relatively better charge transfer by providing a substantial thermodynamic driving force and interfacial electric field.<sup>6,16</sup> However, the  $\text{WO}_3/\text{BiVO}_4$  heterojunction suffers from slow charge transfer (sub  $\mu\text{s}$ ) from  $\text{BiVO}_4$  to  $\text{WO}_3$  due to poor charge transport properties of  $\text{BiVO}_4$  and the presence of recombination centers at the heterojunction interface.<sup>8,17</sup> For such issues, adding an interfacial layer between the  $\text{WO}_3/\text{BiVO}_4$  heterojunction is a promising approach to reduce the interfacial charge recombination and promote charge transfer.

In the present study, a multifaceted approach was implemented for addressing the interfacial charge recombination in the  $\text{WO}_3/\text{BiVO}_4$  heterojunction where (i)  $\text{BiVO}_4$  was co-doped and (ii) an interfacial layer was implemented to improve the effective charge separation and transfer. Initially,  $\text{BiVO}_4$  was co-doped with  $\text{Ga}^{3+}$  and  $\text{W}^{6+}$  at the  $\text{Bi}^{3+}$  and  $\text{V}^{5+}$  sites, respectively, to enhance the light absorption, concentration of photo-generated charge carriers, and improve bulk charge separation. A uniquely prepared sulfur (S) modified  $\text{Bi}_2\text{O}_3$  (S: $\text{Bi}_2\text{O}_3$ ) layer was implemented so that S diffused to the adjacent underlayer ( $\text{WO}_3$ ) and overlayer ((Ga,W): $\text{BiVO}_4$ ), which helped in increasing the number of additional reactive sites for charge transport. Energy-dispersive X-ray analysis (EDAX), X-ray photoelectron spectroscopy (XPS) and time-of-flight secondary ion mass spectrometry (TOF-SIMS) depth profiling were used to determine the qualitative and uniform distribution of sulfur in all layers. The PCD increased from  $2.8 \pm 0.12$  to  $4.0 \pm 0.2$   $\text{mA cm}^{-2}$  for  $\text{WO}_3/(\text{Ga,W}):\text{BiVO}_4$  and  $\text{WO}_3/\text{S}:\text{Bi}_2\text{O}_3/(\text{Ga,W}):\text{BiVO}_4$ , respectively. Additionally, the photocurrent increased to  $5.1 \pm 0.25$   $\text{mA cm}^{-2}$  after adding cobalt phosphate (Co-Pi) to yield a hydrogen generation rate of  $67.3 \mu\text{mol h}^{-1} \text{cm}^{-2}$  for the  $\text{WO}_3/\text{S}:\text{Bi}_2\text{O}_3/(\text{Ga,W}):\text{BiVO}_4/\text{Co-Pi}$  photoanode at  $1.23 V_{\text{RHE}}$  in  $\text{K}_2\text{HPO}_4$  (KPi) under simulated AM 1.5G illumination. Time-resolved photoluminescence (TRPL) and in *operando* femto- and nano-second transient absorption spectroscopy (fs- and ns-TA) results are consistent with more holes being rapidly directed to the reactive surface initially and fast electron transfer occurring from (Ga,W): $\text{BiVO}_4$  to S: $\text{Bi}_2\text{O}_3$  in the ps–ns and from S: $\text{Bi}_2\text{O}_3$  to  $\text{WO}_3$  in the ns– $\mu\text{s}$  time scale. From the detailed analysis, we show that the insertion of a S: $\text{Bi}_2\text{O}_3$  interfacial layer resulted in the best charge separation and transfer kinetics, as well as reduced interfacial recombination sites for all architectures tested. The achieved results are among the highest reported photocurrent densities and hydrogen production rates in the literature.

## 2. Experimental

### 2.1 Thin film fabrication

The  $\text{BiVO}_4$  based thin films were fabricated on a  $1 \times 1 \text{ cm}^2$  fluorine-doped tin oxide (FTO) glass substrate (Aldrich Chemistry: 2.3 mm thick,  $\sim 7 \Omega \text{ sq}^{-1}$  surface resistivity) using

ultrasonic spray coating (Sono-Tek Corporation, USA). A precursor solution of  $\text{BiVO}_4$  was prepared by dissolving 3 mM  $\text{Bi}(\text{NO}_3)_3 \cdot 5\text{H}_2\text{O}$  (Alfa-Aesar, CAS#10035060) and 3 mM  $\text{NH}_4\text{VO}_3$  (Sigma-Aldrich, CAS#7803556) in 2 M  $\text{HNO}_3$  (Sigma-Aldrich, CAS#7803556). The precursor solution was sprayed at a flow rate of  $0.1 \text{ ml min}^{-1}$  for 4 cycles over a FTO substrate held at  $70^\circ\text{C}$ , and then annealed for 10 min at  $500^\circ\text{C}$  in a furnace (Thermo Scientific Thermolyne, model: F48028). The annealed film was sprayed for an additional 4 cycles to obtain the optimized film thickness and then annealed at  $500^\circ\text{C}$  for 2 h. Ga doping was performed by dissolving 3 mM  $\text{Ga}(\text{NO}_3)_3 \cdot x\text{H}_2\text{O}$  (Sigma-Aldrich, CAS#69365726) in the  $\text{BiVO}_4$  precursor solution to get various  $\text{Bi}_{1-x}\text{Ga}_x\text{VO}_4$  compositions (where  $x = 0.01$ – $0.06$  and  $x = 0.04$  were found to be optimal) (Fig. S1a†). W doping was carried out non-stoichiometrically<sup>15</sup> by mixing 3 mM  $(\text{NH}_4)_{10}\text{H}_2(\text{W}_2\text{O}_7)_6$  (Sigma-Aldrich, CAS#11140775) in the  $\text{BiVO}_4$  precursor solution to acquire  $\text{BiV}_{0.992}\text{W}_{0.013}\text{O}_4$  (termed W: $\text{BiVO}_4$ ). The simultaneous co-doping of  $\text{BiVO}_4$  with Ga and W was executed by taking the required amount of gallium nitrate and ammonium tungstate in  $\text{BiVO}_4$  precursor solution to obtain  $\text{Bi}_{0.96}\text{Ga}_{0.04}\text{V}_{0.992}\text{W}_{0.013}\text{O}_4$  (termed (Ga,W): $\text{BiVO}_4$ ).

$\text{WO}_3$  films were fabricated by dissolving 3 mM  $(\text{NH}_4)_{10}\text{H}_2(\text{W}_2\text{O}_7)_6$  (Sigma-Aldrich, CAS#10031513) in 2 M  $\text{HNO}_3$  (Sigma-Aldrich, CAS#7803556). The precursor solution was sprayed for 4 cycles over the FTO substrate (kept at  $40^\circ\text{C}$ ) at a flow rate of  $0.1 \text{ ml min}^{-1}$  using an ultrasonic spray coating tool. The film was annealed at  $500^\circ\text{C}$  for 2 h in air to obtain a thin adherent  $\text{WO}_3$  film. (Ga,W): $\text{BiVO}_4$  was then sprayed over the  $\text{WO}_3$  film to form  $\text{WO}_3/(\text{Ga,W}):\text{BiVO}_4$ .

The precursor solution of  $\text{Bi}_2\text{O}_3$  was prepared by dissolving 1 mM  $\text{Bi}(\text{NO}_3)_3 \cdot 5\text{H}_2\text{O}$  (Alfa-Aesar, CAS#10035060) in 10 ml acetic acid (Sigma-Aldrich, CAS#64197). The  $\text{WO}_3/\text{Bi}_2\text{O}_3$  film was fabricated by ultrasonically spraying the  $\text{Bi}_2\text{O}_3$  precursor solution on the  $\text{WO}_3$  film (kept at  $70^\circ\text{C}$ ) for 3 cycles. The  $\text{WO}_3/\text{Bi}_2\text{O}_3$  bilayer was then annealed at  $500^\circ\text{C}$  for 2 h in air. (Ga,W): $\text{BiVO}_4$  was subsequently sprayed (as discussed) to form  $\text{WO}_3/\text{Bi}_2\text{O}_3/(\text{Ga,W}):\text{BiVO}_4$ .

Fig. 1 and S1b† show a schematic of the  $\text{WO}_3/\text{S}:\text{Bi}_2\text{O}_3/(\text{Ga,W}):\text{BiVO}_4/\text{Co-Pi}$  film fabrication process. The sprayed  $\text{Bi}_2\text{O}_3$  film was immersed in 35 ml methanol (Sigma-Aldrich, CAS#67561) and 0.4 mM dibenzyl disulfide (Alfa Aser, CAS#150607) for 20 min and then annealed in sulfur vapor using a tube furnace (Thermo Scientific Thermolyne, model: HTF55322C). Sulfur vapor was generated by heating 2.5 g of sulfur powder (Alfa Aser, CAS#7704349) at  $120^\circ\text{C}$  in the tube furnace's upstream section. Argon (purity: 99.99%) was used as a carrier gas for the sulfur vapor downstream where the thin film was placed in the hot zone of the tube furnace at  $445^\circ\text{C}$  in air for 1 h to incorporate S into  $\text{Bi}_2\text{O}_3$  (termed S: $\text{Bi}_2\text{O}_3$ ). In the final step, the sulfur-rich film with the  $\text{WO}_3$  layer was used as a substrate to spray (Ga,W): $\text{BiVO}_4$  precursor solution and annealed in air at  $500^\circ\text{C}$  for 2 h to obtain the  $\text{WO}_3/\text{S}:\text{Bi}_2\text{O}_3/(\text{Ga,W}):\text{BiVO}_4$  film.

A co-catalyst Co-Pi was photo-electrodeposited by dissolving 0.1 M  $\text{K}_2\text{HPO}_4$  (Sigma-Aldrich, CAS#7758114) and 0.5 mM  $\text{Co}(\text{NO}_3)_2 \cdot 6\text{H}_2\text{O}$  (Sigma-Aldrich, CAS#10026229) in DI water at

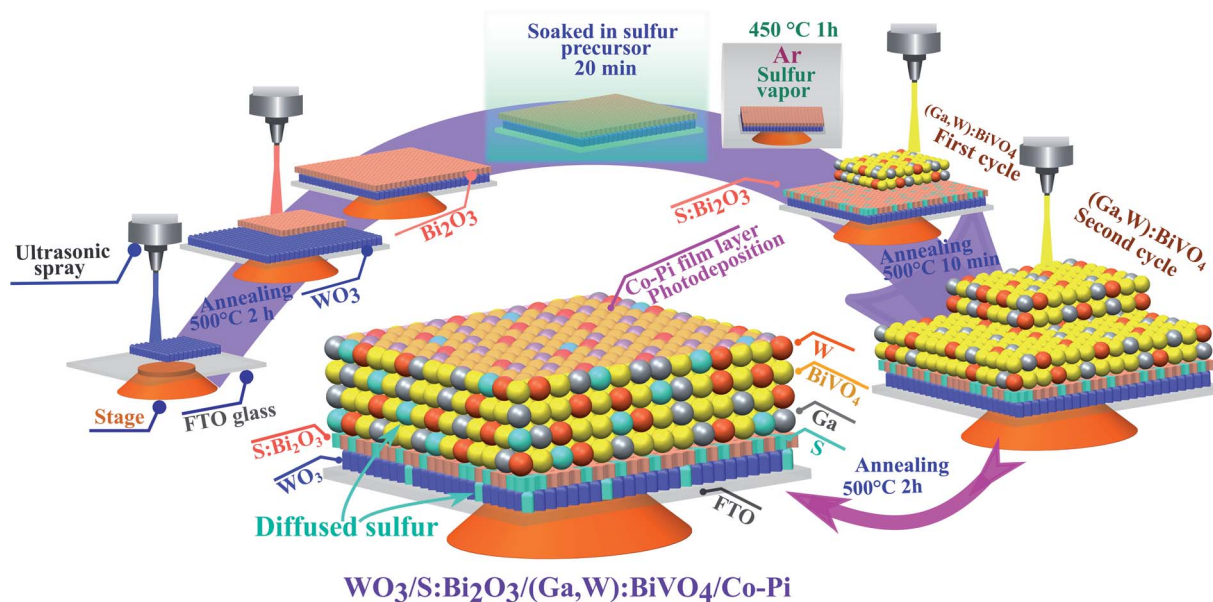


Fig. 1 Schematic illustration of the WO<sub>3</sub>/S:Bi<sub>2</sub>O<sub>3</sub>/(Ga,W):BiVO<sub>4</sub>/Co-Pi film fabrication process.

0.71 V<sub>Ag/AgCl</sub> for 30 s under simulated AM 1.5G illumination to obtain WO<sub>3</sub>/S:Bi<sub>2</sub>O<sub>3</sub>/(Ga,W):BiVO<sub>4</sub>/Co-Pi.

## 2.2 Material characterization

The morphology and elemental spatial distribution of the prepared samples were characterized using a field emission scanning electron microscope (FE-SEM, JEOL 7000F) equipped with EDAX at 25 kV. To investigate the chemical migration that occurs during the sample synthesis process, time of flight secondary ion mass spectrometry TOF-SIMS depth profiling was performed on films at various stages of the annealing process utilizing an ION-TOF TOF-SIMS V spectrometer. The analysis was completed using a 3-lens 30 kV BiMn primary ion gun (30 keV) Bi<sup>+</sup> analysis beam at 1 pA pulsed beam current, where a 50 × 50 μm area was analyzed while the dose density was kept below 1 × 10<sup>12</sup> ions cm<sup>-2</sup> to remain under the static SIMS limit. Sputter depth profiling was accomplished with a 3 kV cesium ion beam (20 nA sputter current) with a raster of 100 × 100 microns.

UV-visible spectroscopy was carried out using an Agilent Technologies (Model: Cary 6000i) optical spectrophotometer. XPS spectra were acquired with a 180° double-focusing hemispherical analyzer with a 128-channel detector using non-monochromatic Al K $\alpha$  radiation as the X-ray source (1486 eV) (Thermo Scientific™ K-Alpha™ X-ray Photoelectron Spectrometer System; VG 220i-XL). This X-ray source beam (diameter: ~0.4 mm) was chosen to minimize the superposition of photoelectron and Auger lines of essential elements. The energy resolution was 0.73 eV with a sufficiently small broadening of natural core level lines and a reasonable signal-to-noise ratio. The binding energy scale was calibrated using C 1s peak at 285 eV, giving an accuracy of 0.1 eV. For depth profiling, a Thermo K-Alpha spectrometer was used with a flood gun for charge

compensation and sputtering was carried out with a raster 2 mm in diameter using Ar sputtering at 3 keV. An X-ray beam with a 35 μm diameter was used every 60 s up to 200 cycles of etching. S 2s peaks were used for S concentration due to the high interference between S 2p and Bi 4f peaks. However, due to the very low relative sensitivity factor of S 2s, the signal-to-noise ratio is relatively low at the given S doping level as compared to that of the other elements, making the error range relatively larger. TRPL measurements were carried out using a setup similar to that described by Kuciauskas *et al.*<sup>18</sup> A PicoQuant 405 nm diode laser generated short pulses (pulse width: ~130 ps) with a repetition rate of 1 MHz, beam spot size of 50 μm and 11 μW power. A fibre-coupled avalanche photodiode with a time resolution of 40 ps was used as the detector. The photon counting rate was maintained at approximately 1% of the repetition rate. Lifetime values were calculated by fitting the decay section of each curve with a biexponential function.

Femto- and nano-second transient absorption spectroscopy (fs- and ns-TAS) was conducted with a Helios Fire spectrometer (Ultrafast Systems), employing a Pharos amplified laser (Light Conversion) as the excitation source. The Pharos was operated at 4 kHz and 4 W power, along with a small portion directed to a sapphire crystal to generate a supercontinuum probe (900–1600 nm). The pump wavelength was tuned to 430 nm with an Orpheus optical parametric amplifier and attenuated with neutral density filters to approximately 150 nJ before being directed to the sample with a spot size of ~0.5 mm. The probe was overlapped with the pump at the sample position and was detected with an InGaAs photodiode array, and photoinduced transmission changes were established by modulating the pump at 2 kHz and subtracting “pump off” from “pump on” probe spectra. The data were adjusted for chirp and background scatter using Surface Explorer. The ns–ms TA was performed with the same excitation beam but with an electronically

delayed supercontinuum probe (Ultrafast System, EOS) to achieve longer delay times. The *in operando* TA measurements were conducted at open circuit potential by placing the sample in a quartz cell in KPi electrolyte. The applied potential was controlled using a Pine WaveNow (Pine Research) Potentiostat/Galvanostat.

### 2.3 Photoelectrochemical measurements

Photoanodes were constructed from the prepared thin films by attaching a copper wire to the FTO, and silver paint was used to establish electrical contact. Epoxy (Loctite 9460) was applied to secure the connection and cover the copper wire, silver paint, and FTO edges. The PEC performance of the photoanodes was evaluated in a standard three-electrode configuration using Pt wire (Premion 99.997%) and Ag/AgCl (3 M NaCl filling solution) as the counter and reference electrodes, respectively. A solar simulator (Sun 3000, model#11000A, ABET Technologies, USA) was used as the light source. Simulated AM 1.5G illumination was established using a GaInP (bandgap: 1.8 eV) photovoltaic primary reference cell. Potentiostat/galvanostat (BioLogic SP-300) was used for photoelectrochemical (PEC) measurements in 0.1 M KPi solution in water (pH = 8.0). The electrolyte was degassed with N<sub>2</sub> gas for about 20 min before every measurement. Incident photon-to-current efficiency (IPCE) measurements were conducted using a 300 W Xe lamp (Newport, 66883), monochromator (Acton SpectraPro-150), mono-Si cell (Hamamatsu) and potentiostat (VersaSTAT 4 Ametek, Princeton Applied Research) with a lock-in amplifier (SR530 Stanford Research System). A 495 nm longpass filter (Newport) was added after the monochromator for wavelengths >550 nm to filter second-order diffractions. Electrochemical impedance spectroscopy (EIS) measurements were performed at a frequency range of 100 kHz to 100 mHz under simulated AM 1.5G illumination.

The H<sub>2</sub> and O<sub>2</sub> gases generated in the PEC process were collected in a three-electrode setup by tracking the electrolyte volume from a filled tube.<sup>19</sup> The faradaic efficiency ( $\eta_{\text{H}_2}$ ) was calculated using,

$$\eta_{\text{H}_2} = \frac{P_{\text{H}_2} V}{RT} \times \frac{1}{(\text{Coulombs passed}) \times (\text{mole } 96485C) \times (\text{mol H}_2 \text{ per } 2 \text{ mole})}$$

where  $P_{\text{H}_2}$ ,  $V$ ,  $R$  and  $T$  are the pressure from H<sub>2</sub> evolution (hPa), volume (L), gas constant (0.08206 L atm K<sup>-1</sup> mol<sup>-1</sup>) and  $T$  temperature (K), respectively.  $P_{\text{H}_2}$  was calculated by subtracting the water vapor pressure ( $P_{\text{H}_2\text{O vapor}}$ ) and pressure from the suspended solution ( $P_{\text{suspended}}$ ) from atmospheric pressure ( $P_{\text{atm}}$ ) measured using a barometer.

$$P_{\text{H}_2} = P_{\text{atm}} - P_{\text{H}_2\text{O vapor}} - P_{\text{suspended}}$$

where,  $P_{\text{suspended}}$  is calculated by measuring the height ( $h_1$ ) of the suspended solution above the solution level in the setup:

$$P_{\text{suspended}} = h_1 \times \frac{\text{Hg density}}{\text{solution density}} \times \frac{1 \text{ atm}}{760 \text{ mm Hg}} \\ = h_1 \times 0.0736 \text{ (torr per mm)}$$

The faradaic efficiency measurement was validated using Pt electrodes as an anode and cathode for electrolysis and obtained  $\eta_{\text{H}_2}$  0.98 ± 0.02. The measurements were conducted at 1.23 V<sub>RHE</sub> in KPi electrolyte under simulated AM 1.5G illumination.

## 3. Results and discussion

### 3.1 Photoelectrochemical and optical measurements

Looking first at films, Fig. 2a and Table S1a† compare the PEC performance of intrinsic BiVO<sub>4</sub> (i-BiVO<sub>4</sub>), Ga:BiVO<sub>4</sub>, W:BiVO<sub>4</sub> and (Ga,W):BiVO<sub>4</sub> under chopped light up to 2.4 V<sub>RHE</sub>. Ga:BiVO<sub>4</sub> exhibited a photocurrent density of 0.4 ± 0.02 mA cm<sup>-2</sup>, which is almost twice that of i-BiVO<sub>4</sub> (0.25 ± 0.01 mA cm<sup>-2</sup>); this improvement is attributed to the increased Fermi-level splitting and therefore decreasing carrier recombination *via* incorporation of Ga<sup>3+</sup> at Bi<sup>3+</sup> sites.<sup>20</sup> Similarly, W:BiVO<sub>4</sub> exhibited enhanced PCD (1.02 ± 0.04 mA cm<sup>-2</sup>) of over four times that of i-BiVO<sub>4</sub>, which is attributed to the increased carrier concentration of W<sup>6+</sup> donors at V<sup>5+</sup> sites.<sup>21</sup> Finally, (Ga,W):BiVO<sub>4</sub> demonstrated superior (~7 times) PEC performance (1.68 ± 0.1 mA cm<sup>-2</sup>) compared to i-BiVO<sub>4</sub>, likely due to the combined effects of Ga and W doping.

Next, the PEC performance of heterojunctions was evaluated (Fig. 2b, S2a and Table S1b†). Based on Fig. 2a, (Ga,W):BiVO<sub>4</sub> was selected to form a type-II heterojunction with WO<sub>3</sub>. By doing so, the WO<sub>3</sub>/(Ga,W):BiVO<sub>4</sub> photoanode exhibited a photocurrent density of 2.8 ± 0.12 mA cm<sup>-2</sup>, which nearly doubled compared to (Ga,W):BiVO<sub>4</sub>, likely due to the improved light absorption at  $\lambda \leq 450$  nm, charge transfer kinetics and reduced recombination sites.<sup>22,23</sup> However, the WO<sub>3</sub>/BiVO<sub>4</sub> interface is also known to have a high defect density, which can lead to significant recombination and slow charge transport.<sup>8,17</sup> Therefore, a thin layer of bismuth oxide (Bi<sub>2</sub>O<sub>3</sub>) was inserted at the WO<sub>3</sub>/BiVO<sub>4</sub> interface. While Bi<sub>2</sub>O<sub>3</sub> has appropriate band alignment to promote charge transfer (validated in Fig. S2b†), the PEC measurement was not significantly enhanced relative to WO<sub>3</sub>/(Ga,W):BiVO<sub>4</sub> (only 1.2 times higher), likely due to the higher levels of recombination in this layer.<sup>24</sup> Therefore, sulfur (S) was incorporated into Bi<sub>2</sub>O<sub>3</sub> such that, along with passivating the Bi<sub>2</sub>O<sub>3</sub> bulk, S also diffused into the adjacent WO<sub>3</sub> and (Ga,W):BiVO<sub>4</sub> layers (Fig. 2b and S2c†). Sulfur is expected to enhance water oxidation by generating oxygen vacancies and forming new reaction sites that help charge migration/separation and reduce carrier recombination.<sup>25,26</sup> The optimized WO<sub>3</sub>/S:Bi<sub>2</sub>O<sub>3</sub>/(Ga,W):BiVO<sub>4</sub> photoanode demonstrated an excellent photocurrent density of 4.0 ± 0.2 mA cm<sup>-2</sup> at 1.23 V<sub>RHE</sub> which was ~1.2 and ~1.5 times higher than that of the WO<sub>3</sub>/Bi<sub>2</sub>O<sub>3</sub>/(Ga,W):BiVO<sub>4</sub> and WO<sub>3</sub>/(Ga,W):BiVO<sub>4</sub> photoanodes, respectively.

A surface catalyst (Co-Pi) deposited WO<sub>3</sub>/S:Bi<sub>2</sub>O<sub>3</sub>/(Ga,W):BiVO<sub>4</sub>/Co-Pi photoanode exhibited a remarkably high

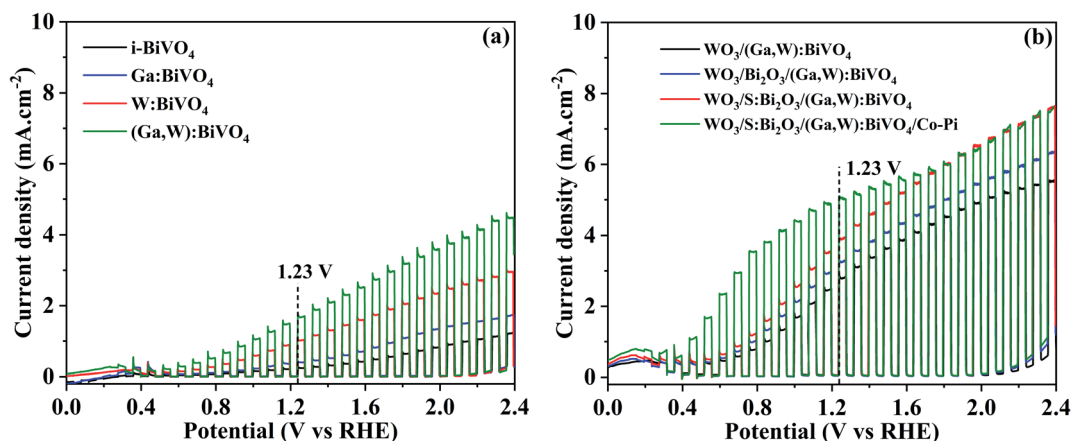


Fig. 2  $J$ - $V$  plots under simulated AM 1.5G illumination in KPi for photoanodes (a) Ga, W doped and (Ga,W) co-doped along with  $i$ - $\text{BiVO}_4$  and (b) with the  $\text{WO}_3$  heterojunction and  $\text{Bi}_2\text{O}_3$  interface layer without and with sulfur modification.

photocurrent density of  $5.1 \pm 0.25 \text{ mA cm}^{-2}$  at  $1.23 \text{ V}_{\text{RHE}}$  in KPi. The Co-Pi layer facilitates hole collection at the photoanode/electrolyte interface to participate in the water oxidation reaction.<sup>5</sup> The photocurrent measurement with the hole scavenger and the Mott-Schottky analysis at different frequencies are discussed in the ESI (Sections 3 and 4).†

The spectral response was investigated to understand the impact of doping, co-doping and heterojunction formation. From Fig. S5a,† it was observed that doping  $\text{BiVO}_4$  with Ga enhanced total light absorption and extended the onset from  $\sim 520$  to  $\sim 535 \text{ nm}$ . A similar trend was observed for the co-doped (Ga,W): $\text{BiVO}_4$  sample, likely due to the redshift in light absorption caused by Ga doping.<sup>20</sup> There was no substantial change in absorption observed for W doping.<sup>10</sup> Moreover, the light interaction improved by forming a heterojunction with  $\text{WO}_3$  (*i.e.*,  $\text{WO}_3/(\text{Ga,W})\text{:BiVO}_4$ ) where  $\text{WO}_3$  ( $\lambda \leq 450 \text{ nm}$ ) absorbs high energy photons along with modified  $\text{BiVO}_4$  (300–530 nm), which absorb a wide range of photons.  $\text{S:Bi}_2\text{O}_3$  ( $\lambda \leq 430$ ) further improved the light absorption of  $\text{WO}_3/\text{S:Bi}_2\text{O}_3/(\text{Ga,W})\text{:BiVO}_4$  compared to that of  $\text{WO}_3/\text{Bi}_2\text{O}_3/(\text{Ga,W})\text{:BiVO}_4$  due to the formation of interband on S modification which causes the

redshift in the light absorption.<sup>24,25</sup> The respective absorption efficiencies ( $\phi_{\text{abs}}$ ) were calculated by integrating the absorption spectra from 300 to 550 nm for all samples, as indicated in Fig. 3a and S5a†: inset. The measured bandgaps were 2.71 and 2.8 eV (Fig. S5b†) for  $\text{WO}_3$  and  $\text{Bi}_2\text{O}_3$ , respectively. There was a slight ( $\sim 0.04 \text{ eV}$ ) reduction in the optical bandgap of Ga: $\text{BiVO}_4$  (2.39 eV) and (Ga,W): $\text{BiVO}_4$  (2.38 eV) compared to that of  $i$ - $\text{BiVO}_4$  (2.42 eV), which was expected due to the redshift in the absorption edge upon Ga doping. Bulk charge separation and surface charge transfer efficiencies are discussed in the ESI (Section 5, Fig. S5c-f†).

The quantification of the absorbed photons undergoing photoactivity corresponding to the wavelength was determined from the IPCE. The measurements for all heterojunction based photoanodes were conducted at  $1.23 \text{ V}_{\text{RHE}}$  (Fig. 3b). The  $\text{WO}_3/\text{S:Bi}_2\text{O}_3/(\text{Ga,W})\text{:BiVO}_4$  photoanode showed a maximum IPCE value of  $63 \pm 3\%$ , followed by  $\text{WO}_3/\text{Bi}_2\text{O}_3/(\text{Ga,W})\text{:BiVO}_4$  ( $52 \pm 2\%$ ) and  $\text{WO}_3/(\text{Ga,W})\text{:BiVO}_4$  ( $42 \pm 1.6\%$ ), respectively at 460 nm. The  $\text{WO}_3/\text{S:Bi}_2\text{O}_3/(\text{Ga,W})\text{:BiVO}_4$  photoanode with Co-Pi exhibited the highest IPCE ( $72 \pm 3.2\%$ ). The IPCE was integrated over the AM1.5G reference spectrum, and the resulting photocurrent

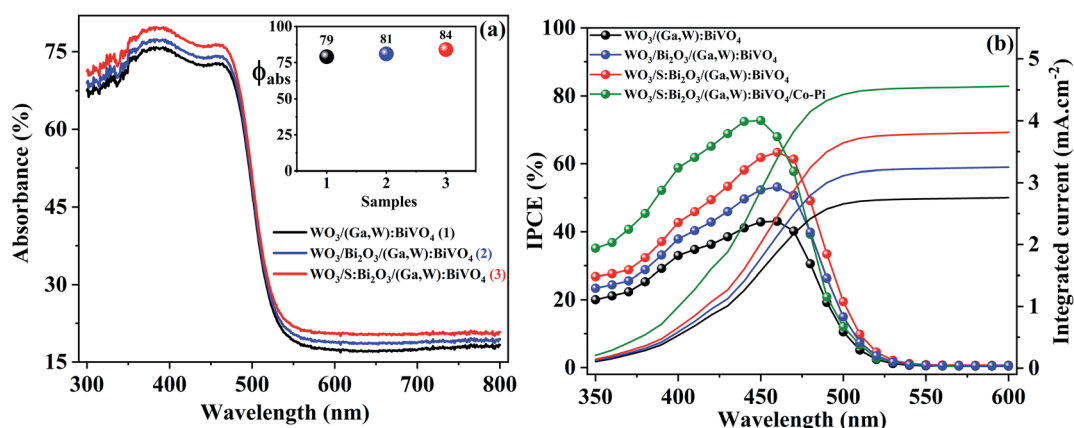


Fig. 3 (a) Absorption spectra (inset: absorption efficiency), (b) incident photon-to-current efficiency, measured at  $1.23 \text{ V}_{\text{RHE}}$  in KPi electrolyte for photoanodes with the  $\text{WO}_3$  heterojunction and  $\text{Bi}_2\text{O}_3$  interface layer without and with sulfur modification.

densities for each sample (Fig. 3b) agreed with those measured under simulated AM 1.5G illumination at 1.23  $V_{RHE}$  (Fig. 2b). A small variation ( $\sim 5\%$ ) in the photocurrent measured by LSV and integrated current from IPCE is a general phenomenon due to measuring uncertainty.

### 3.2 Surface morphology, crystal structure and elemental analysis of thin films

To better understand the PEC performance trends, the physicochemical characterization of intrinsic and doped samples was carried out to evaluate the morphology, elemental mapping, crystal structure and oxidation state. The SEM images in Fig. S6a–c† show that  $i\text{-BiVO}_4$ ,  $\text{WO}_3$  and  $\text{Bi}_2\text{O}_3$  have a planar structure with uniform nanoporous morphology. Fig. 4a shows that after co-doping the  $i\text{-BiVO}_4$  film with Ga and W, the overall porosity increased substantially without changing the grain size (50–200 nm). The inset image illustrates the uniform growth of nano-sized grains, leading to better light absorption and more electrochemical active surface area by increasing the contact area between the film surface and electrolyte. The cross-sectional image (Fig. 4b) of  $\text{WO}_3/\text{S:Bi}_2\text{O}_3/(\text{Ga,W})\text{:BiVO}_4$  showed the uniformly connected nanoporous grains. The layer thicknesses are 200–300, 200–300 and 500–750 nm for the  $\text{WO}_3$ ,  $\text{S:Bi}_2\text{O}_3$  and  $(\text{Ga,W})\text{:BiVO}_4$  layers, respectively. It was observed

that the clear separation of all three layers is difficult as layers amalgamated due to the porous nature of all films. The FTO coating thickness on the glass substrate was  $\sim 50$  nm (Fig. S6d†). The composition and elemental distribution of the as-deposited  $\text{WO}_3/\text{S:Bi}_2\text{O}_3/(\text{Ga,W})\text{:BiVO}_4$  were mapped based on the integrated intensities of peak signals of Bi, V, O, W, Ga and S as a function of beam position using FESEM-EDAX mode. Fig. 4c–h show the uniform distribution of elements Bi, V, O, W, Ga, and S. Consequently, the element spectra in Fig. 4i demonstrates the uniform presence of S along with other elements. In the Fig. 4i inset, Bi and S peaks were deconvoluted to determine the distinct measure of S due to the near overlap of the two peaks. S and Bi peaks were observed at 2.36 and 2.45 keV, respectively. Additionally, the quantification of S was determined to be 2.77 at% from EDAX analysis (Fig. 4i: inset).

The crystal structure was determined using X-ray diffraction (XRD) analysis for intrinsic, doped  $\text{BiVO}_4$ ,  $\text{Bi}_2\text{O}_3$ ,  $\text{WO}_3$  and heterojunction samples without any impurity, complex phases and S peaks (discussed in the ESI, Fig. S7a and b†). The oxidation state of Bi, V, W, Ga and O in the  $\text{WO}_3/\text{S:Bi}_2\text{O}_3/(\text{Ga,W})\text{:BiVO}_4$  sample was determined using surface XPS (discussed in ESI, Fig. S8a–f†). However, subsequently employed XPS depth profiling could not identify S in any layers due to the low concentration of S and detection limit of XPS (Fig. S8g†). In order to determine the oxidation state of sulfur, two distinct

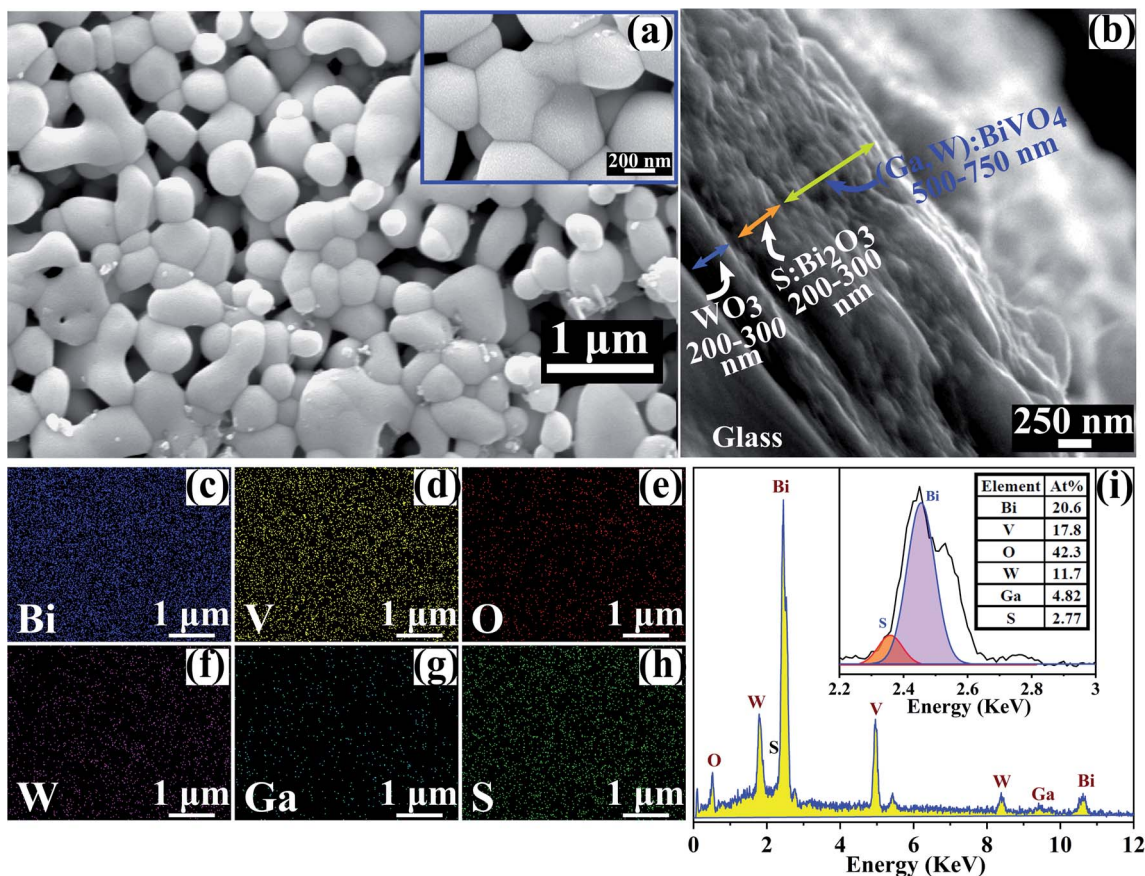


Fig. 4 (a) Surface morphology. (b) Cross-sectional, (c–h) plan view elemental mapping and (i) elemental spectra (inset: deconvolution of Bi and S peaks and at%) of the  $\text{WO}_3/\text{S:Bi}_2\text{O}_3/(\text{Ga,W})\text{:BiVO}_4$  sample.

samples were prepared (Fig. S8h†): intermediate S treated  $\text{WO}_3/\text{Bi}_2\text{O}_3$  and  $\text{WO}_3/\text{S}:\text{Bi}_2\text{O}_3/(\text{Ga,W}):\text{BiVO}_4$  with a high S content (total S treatment to the  $\text{WO}_3/\text{Bi}_2\text{O}_3$  layer was 4 h, 4 times higher than that of the actual sample). From the S 2s spectrum in Fig. 5a, the oxidation state of S was attributed to  $-2$  in the form of  $\text{Bi}_2\text{S}_3$  (224.8 eV) and  $\text{Bi}_2\text{O}_3$  (230.6 and 233.8 eV) peaks for the S treated  $\text{WO}_3/\text{Bi}_2\text{O}_3$  sample.<sup>27</sup> Similarly, the  $\text{WO}_3/\text{S}:\text{Bi}_2\text{O}_3/(\text{Ga,W}):\text{BiVO}_4$  sample with high S content validated  $-2$  states ( $\text{Bi}_2\text{S}_3$  (223.4 eV) and  $\text{Bi}_2\text{O}_3$  (233.3 eV)). However, it is possible that peaks at 233.8 eV and 233.3 eV could also have sulfates or highly oxidized sulfur species ( $\text{SO}_x$ ).<sup>27</sup> Additionally, depth

profiling was performed, as shown in Fig. 5b, for  $\text{WO}_3/\text{S}:\text{Bi}_2\text{O}_3/(\text{Ga,W}):\text{BiVO}_4$  sample with high S content to determine the atomic concentration of Bi 4f, V 2p, O 1s, W 4f, Ga 2p and S 2s with depth. It was observed that the S distribution was uniform throughout the film depth except that it was slightly higher at the film surface. The atomic concentration of S was approximately 12 at% uniformly distributed in the sample with high S content. It may be estimated that sulfur could be approximately 3 at% uniformly distributed in the actual sample considering S diffusion rates as sulfur treatment was 4 times in the high S content sample. The atomic concentration of Bi 4f, V 2p, O 1s,

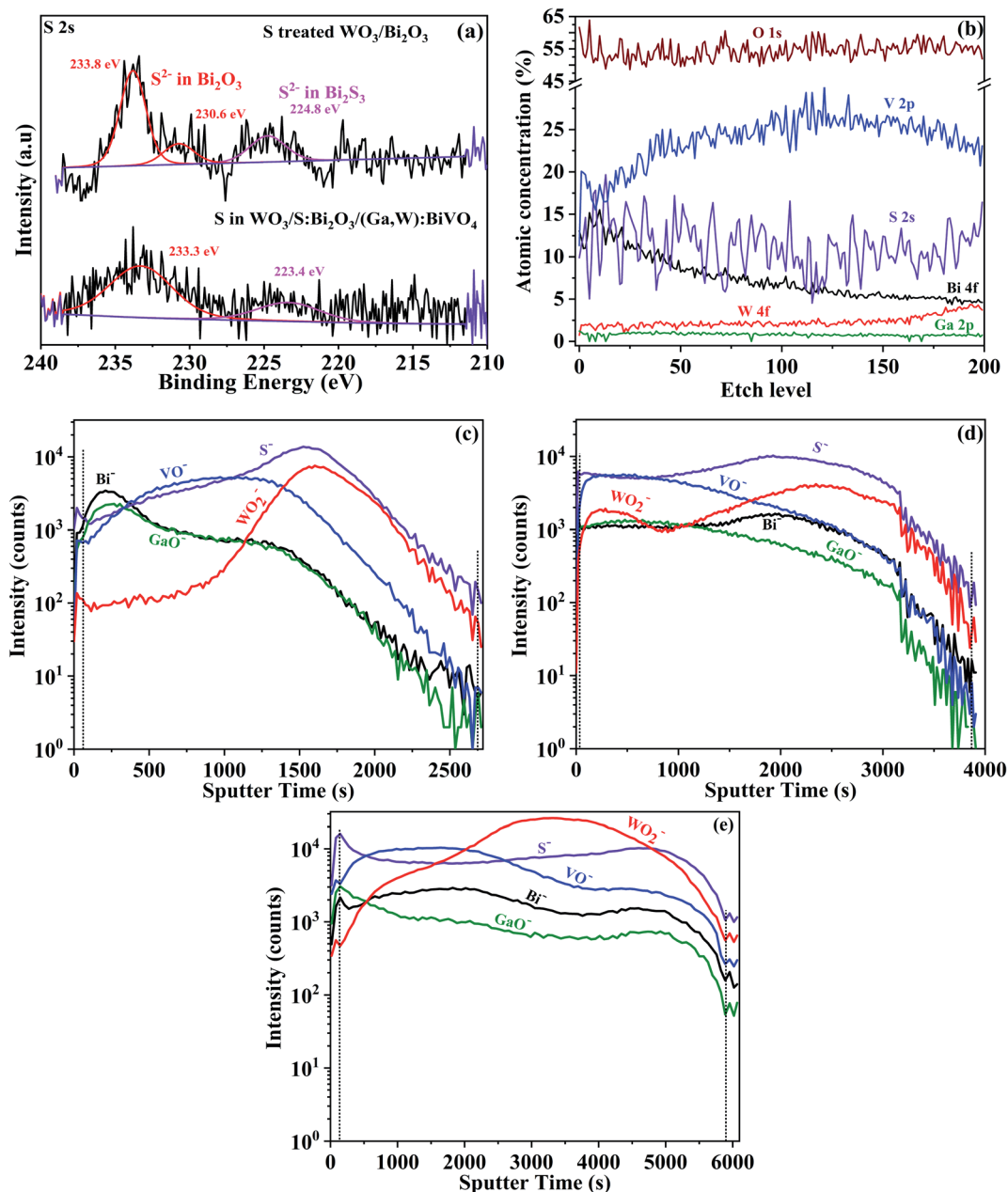


Fig. 5 (a) S 2s XPS spectra of S treated  $\text{WO}_3/\text{Bi}_2\text{O}_3$  and high S concentrated  $\text{WO}_3/\text{S}:\text{Bi}_2\text{O}_3/(\text{Ga,W}):\text{BiVO}_4$  films. (b) XPS depth profiling spectra for the atomic concentration (%) of Bi 4f, V 2p, O 1s, W 4f, Ga 2p and S 2s as a function of the etch level for the  $\text{WO}_3/\text{S}:\text{Bi}_2\text{O}_3/(\text{Ga,W}):\text{BiVO}_4$  film with high S content. Negative polarity TOF-SIMS depth profiles of the  $\text{WO}_3/\text{S}:\text{Bi}_2\text{O}_3/(\text{Ga,W}):\text{BiVO}_4$  sample in three distinct (Fig. S5a†) environments: (c) control (no annealing), (d) short annealing (5 min at 500 °C) and (e) complete annealing (2 h at 500 °C) for  $\text{Bi}^-$ ,  $\text{VO}^-$ ,  $\text{WO}_2^-$ ,  $\text{GaO}^-$  and  $\text{S}^-$  species.

W 4f and Ga 2p was distributed as per the filmstack structure. V 2p and Ga 2p were noticed to have minor diffusion in the adjacent layers, which was possible due to the porous nature of the film.

In order to understand the nature of the sulfur diffusion process in the actual film from the Bi<sub>2</sub>O<sub>3</sub> interfacial layer to the WO<sub>3</sub> and (Ga,W):BiVO<sub>4</sub> adjacent layers, TOF-SIMS depth profiling was employed for the WO<sub>3</sub>/S:Bi<sub>2</sub>O<sub>3</sub>/(Ga,W):BiVO<sub>4</sub> sample under three distinct annealing conditions after (Ga,W):BiVO<sub>4</sub> precursor deposition on the sulfur treated WO<sub>3</sub>/Bi<sub>2</sub>O<sub>3</sub> film. The prepared samples, as shown in Fig. S9a,† were the control (without annealing), short annealed (5 min) and completely annealed (final sample) samples. Secondary ion signals were selected which were of high intensity and represented major components of the various layers in the filmstack. These species were Bi<sup>-</sup>, VO<sup>-</sup>, WO<sub>2</sub><sup>-</sup>, GaO<sup>-</sup> and S<sup>-</sup> which represent Bi, V, W, Ga and S elements, respectively. The layer interface was not measured due to high surface roughness and it was also observed that the clear distinction of each layer was difficult to achieve (Fig. 4b and 5b) due to their porous nature. However, a rough estimation is shown in Fig. S9b-d.† The control sample showed that sulfur was contained to the Bi<sub>2</sub>O<sub>3</sub> layer only, as observed by the pronounced peak of sulfur in the Bi<sub>2</sub>O<sub>3</sub> layer in Fig. 5c. On the contrary, Fig. 5d showed that even on short annealing of 5 min at 500 °C, significant migration of sulfur occurred as the sulfur distribution migrated significantly into the (Ga,W):BiVO<sub>4</sub> and WO<sub>3</sub> layers, also noted from the significant broadening of the sulfur trace. Subsequently, in Fig. 5e, a completely annealed sample (2 h time at 500 °C) showed that the sulfur distribution was uniform throughout the film thickness, which was also corroborated by EDAX analysis (Fig. 4c-i) and XPS depth profiling (Fig. 5b). However, the sulfur content was higher on the (Ga,W):BiVO<sub>4</sub> surface, possibly due to the small deposition of sulfur during migration from the Bi<sub>2</sub>O<sub>3</sub> layer and a similar behavior was observed in the XPS depth profiling (Fig. 5b). It was assumed that sulfur was passivated in all grain boundaries and surfaces/interfaces/defects throughout all layers, rather than being a bulk alloy element. Along with sulfur, a less extreme amount of diffusion observed for the Bi, V, W and Ga components in the film thickness (Fig. 5c-e) may be due to the highly porous nature of the film (Fig. 4a) and a similar behavior was observed in the XPS depth profiling. The distribution of the substrate elements (F<sup>-</sup>, Sn<sup>-</sup> and Si<sup>-</sup>) is shown in Fig. S9b-d.†

### 3.3 Electrochemical impedance analysis

Fig. 6a shows the impedance patterns of photoanodes with the WO<sub>3</sub> heterojunction and Bi<sub>2</sub>O<sub>3</sub> interface layer without and with sulfur modification. The WO<sub>3</sub>/(Ga,W):BiVO<sub>4</sub> photoanode shows lower impedance than WO<sub>3</sub>/Bi<sub>2</sub>O<sub>3</sub>/(Ga,W):BiVO<sub>4</sub> in the low-frequency region. Interestingly, the WO<sub>3</sub>/S:Bi<sub>2</sub>O<sub>3</sub>/(Ga,W):BiVO<sub>4</sub> photoanode demonstrated even lower real impedance at a lower frequency than WO<sub>3</sub>/Bi<sub>2</sub>O<sub>3</sub>/(Ga,W):BiVO<sub>4</sub>. Resistance and capacitance in the bulk and at the surface were evaluated as a function of voltage using the Randles circuit (Fig. S10a & b†), which consists of resistance related to connections ( $R_{\text{series}}$ ), bulk

resistance ( $R_{\text{bulk}}$ ), surface resistance ( $R_{\text{surface}}$ ), bulk capacitance ( $C_{\text{bulk}}$ ) and surface capacitance ( $C_{\text{surface}}$ ) connected to a Helmholtz layer at the photoanode and electrolyte interface. Fig. 6b shows that  $R_{\text{bulk}}$  and  $R_{\text{surface}}$  tend to drop gradually until  $\sim 1 V_{\text{RHE}}$  after which, the photocurrent was mainly controlled by photogenerated holes reaching the surface.<sup>28</sup>  $R_{\text{bulk}}$  followed the order of WO<sub>3</sub>/S:Bi<sub>2</sub>O<sub>3</sub>/(Ga,W):BiVO<sub>4</sub> < WO<sub>3</sub>/Bi<sub>2</sub>O<sub>3</sub>/(Ga,W):BiVO<sub>4</sub> < WO<sub>3</sub>/(Ga,W):BiVO<sub>4</sub>. The evaluated capacitance of photoanodes shown in Fig. 6c illustrated that  $C_{\text{bulk}}$  decreases with increasing potential and exhibits less recombination in the bulk and facilitated charge transfer. The  $C_{\text{surface}}$  gradually increased with potential, and followed the trend of WO<sub>3</sub>/S:Bi<sub>2</sub>O<sub>3</sub>/(Ga,W):BiVO<sub>4</sub> > WO<sub>3</sub>/Bi<sub>2</sub>O<sub>3</sub>/(Ga,W):BiVO<sub>4</sub> > WO<sub>3</sub>/(Ga,W):BiVO<sub>4</sub>. The interfacial layer with S enhanced the charge transfer rate, facilitated the charge accumulation and transport by reducing the density of surface trapped holes in the bulk and the surface.

The total resistance ( $R_{\text{tot}}$ ), which represents the combination of charge transport (bulk) and interfacial charge transfer (surface), was evaluated using  $R_{\text{tot}} = \left(\frac{dI}{dV}\right)^{-1}$  in Fig. 6d. A valley was observed at  $\sim 1 V_{\text{RHE}}$  for all photoanodes (fitting curve is shown in Fig. S10c†). A cathodic shift of 164.3 and 33.5 mV in the valley implied higher charge extraction and a decrease in the  $R_{\text{tot}}$  of 39.2 and 12  $\Omega \text{ cm}^{-2}$  for WO<sub>3</sub>/S:Bi<sub>2</sub>O<sub>3</sub>/(Ga,W):BiVO<sub>4</sub> and WO<sub>3</sub>/S:Bi<sub>2</sub>O<sub>3</sub>/(Ga,W):BiVO<sub>4</sub>, respectively, compared to that of WO<sub>3</sub>/(Ga,W):BiVO<sub>4</sub> indicated the reduced bulk recombination (indicated in Fig. 6b).<sup>28,29</sup> Both of these criteria best fit for the WO<sub>3</sub>/S:Bi<sub>2</sub>O<sub>3</sub>/(Ga,W):BiVO<sub>4</sub> photoanode, confirming the higher charge separation and transfer rate. The close relationship was demonstrated with  $R_{\text{tot}}$  calculated from the  $I-V$  ( $R_{\text{tot}} = \left(\frac{dI}{dV}\right)^{-1}$ ) and impedance measurements ( $R_{\text{tot}} = R_{\text{bulk}} + R_{\text{surface}}$ ), as shown in Fig. 6d. This excellent agreement substantiates the photocurrent obtained from the experiment.

### 3.4 Time-resolved study of charge dynamics

The photogenerated charge carrier dynamics and kinetics were explored by TRPL measurements of the WO<sub>3</sub>/(Ga,W):BiVO<sub>4</sub> and WO<sub>3</sub>/S:Bi<sub>2</sub>O<sub>3</sub>/(Ga,W):BiVO<sub>4</sub> samples. Fig. 7a shows the PL intensity decay after exciting the thick (Ga,W):BiVO<sub>4</sub> layer and likely produces excited states in this layer using a laser source centered at 405 nm. The PL decay ( $I(t)$ ) was fit with a second-order exponential function  $I(t) = A_1 \exp\left(-\frac{t}{\tau_1}\right) + A_2 \exp\left(-\frac{t}{\tau_2}\right)$ , where  $A_1$  and  $A_2$  are amplitudes of components with lifetimes  $\tau_1$  and  $\tau_2$ , respectively.<sup>30</sup> The average PL lifetime ( $\langle\tau\rangle$ ) of each sample was calculated using  $\langle\tau\rangle = \frac{A_1\tau_1^2 + A_2\tau_2^2}{A_1\tau_1 + A_2\tau_2}$  (all calculated parameters are presented in Table S2†). The average carrier lifetimes of WO<sub>3</sub>/(Ga,W):BiVO<sub>4</sub> and WO<sub>3</sub>/S:Bi<sub>2</sub>O<sub>3</sub>/(Ga,W):BiVO<sub>4</sub> were  $0.477 \pm 0.05$  and  $0.418 \pm 0.04$  ns, respectively. Interestingly, the two dominant benefits which are expected from S:Bi<sub>2</sub>O<sub>3</sub> incorporation (*i.e.*, reduced recombination and fast charge transport) have competing effects on the carrier lifetime, where reduced recombination increases the lifetime while fast charge

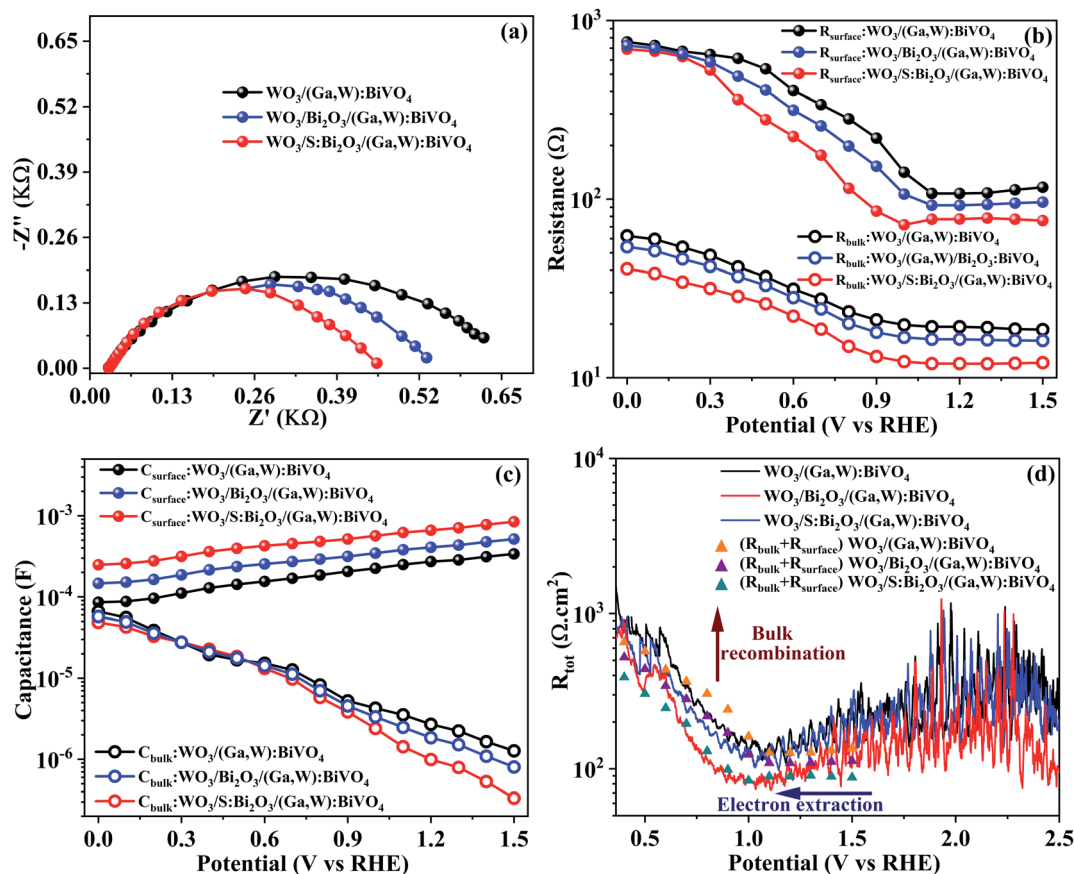


Fig. 6 (a) Nyquist plots measured in KPi at 1.23  $V_{RHE}$  under simulated AM 1.5G illumination, (b)  $R_{surface}$  (solid markers),  $R_{bulk}$  (open markers), (c)  $C_{surface}$  (solid markers) and  $C_{bulk}$  (open markers) determined using the Randles circuit (Fig. S10a & b†) for photoanodes with the  $WO_3$  heterojunction and  $Bi_2O_3$  interface layer without (blue) and with (red) sulfur modification. (d)  $R_{tot}$  (line) calculated using  $\left(\frac{dI}{dV}\right)^{-1}$  and compared with  $R_{tot}$  (triangles) obtained by impedance ( $R_{tot} = R_{bulk} + R_{surface}$ ) measurements.

transport reduces it. This may be the reason that the lifetime was not found to vary significantly between the two samples. The charge transfer rate constant ( $k_{ct}$ ) can also be calculated using  $k_{ct} = \frac{1}{\langle \tau \rangle}$ .<sup>30</sup> The obtained  $k_{ct}$  for  $WO_3/(Ga,W):BiVO_4$  and  $WO_3/S:Bi_2O_3/(Ga,W):BiVO_4$  were  $2.095 \pm 0.2 \text{ ns}^{-1}$  and  $2.393 \pm 0.22 \text{ ns}^{-1}$ , respectively, suggesting that the enhanced charge transfer may be slightly more dominant.

TA was employed for an in-depth understanding of the charge dynamics behavior across the  $WO_3/(Ga,W):BiVO_4$  interface without and with the  $S:Bi_2O_3$  interfacial layer by placing the sample in air and electrolyte (*operando*). First, fs-TA data were collected for the sample in air, pumped at 430 nm and probed in the range from 900–1400 nm for  $WO_3/(Ga,W):BiVO_4$  and  $WO_3/S:Bi_2O_3/(Ga,W):BiVO_4$  samples. It is believed that this infrared probing range tracks the free and trapped photo-generated carriers, while the excitation first strikes the thick  $(Ga,W):BiVO_4$  layer and likely predominately produces excited states in this layer. The intensity decay curve plotted in Fig. 7b demonstrates faster initial decay on the ps time scale for the  $WO_3/(Ga,W):BiVO_4$  sample compared to that of  $WO_3/S:Bi_2O_3/(Ga,W):BiVO_4$ . This fast decay likely corresponds to the

geminate electron–hole recombination, which is ameliorated with the additional  $Bi_2O_3$  layer, facilitating electron movement away from  $BiVO_4$  and suppressing initial recombination. The recorded decay ( $\Delta A$ ) signal was fitted using the exponential decay model  $\Delta A = \sum_{i=1}^n A_i \exp\left(-\frac{t}{\tau_i}\right)$  where  $A_i$  and  $\tau_i$  are the amplitude and the lifetime of an exponential decay component, respectively. The calculated fitting parameters are summarized in Table S3,† and the values are commensurate with those found in the literature.<sup>9</sup> The fs-TA is best fit with 3 exponentials in the ns regime without an extended component in the microsecond regime due to absence of electrolyte that stabilizes separated charges. Time constants  $\tau_1$ ,  $\tau_2$  and  $\tau_3$  can be inferred as loss of excited states due to hole trapping and the depletion of the trapped holes due to electron–hole recombination with free and thermalized electrons.<sup>9,31</sup> It is inferred from  $\tau_1$  that the initial fast processes leading to carrier loss are reduced in the  $WO_3/S:Bi_2O_3/(Ga,W):BiVO_4$  sample, as all decay time constants are slower than those of the  $WO_3/(Ga,W):BiVO_4$  sample. The subsequent remaining carriers are left to undergo slower interfacial recombination on a ns timescale without electrolyte. We note that unlike TRPL, which only measures radiative

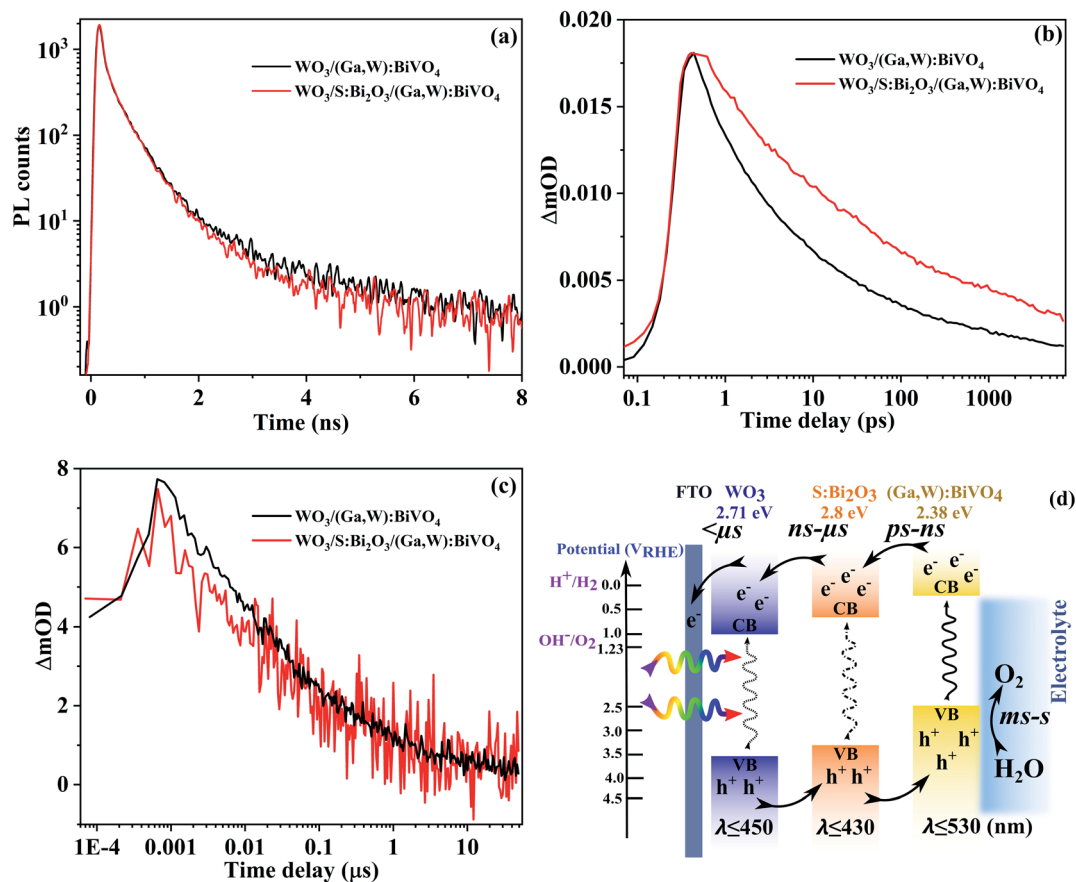


Fig. 7 (a) Time-resolved PL emission (excited at  $\lambda = 405$  nm). TA spectra collected, pumped at 430 nm and probed in the range of 900–1400 nm (b) in air for fs-TA and (c) in KPi electrolyte for ns-TA at an open circuit potential for  $\text{WO}_3/(\text{Ga,W})\text{:BiVO}_4$  and  $\text{WO}_3/\text{S:Bi}_2\text{O}_3/(\text{Ga,W})\text{:BiVO}_4$  photoanodes. (d) Schematic of band alignment for the  $\text{WO}_3/\text{S:Bi}_2\text{O}_3/(\text{Ga,W})\text{:BiVO}_4$  heterojunction illustrating photoactivated charge generation, transfer process and related time scale.

electron–hole recombination and thus separation leads to reduced lifetime, the absorptive TA signal represents carrier population and as such, a persistent signal also indicates carrier motion to avoid recombination.

Next, the ns-TA measurement was conducted with samples submerged in the electrolyte to evaluate hole transfer kinetics at the semiconductor/electrolyte interface. The measurement was conducted at open circuit potential, pumped at 430 nm and probed in the range of 900–1400 nm in KPi electrolyte. It was predicted that at open circuit potential, a partially occupied electron trap state can exhibit optical transition behavior to a localized trap state.<sup>6</sup> The band bending at the photoanode/electrolyte interface can prolong the photogenerated hole lifetime ( $\mu\text{s}$ ) and accumulation.<sup>6</sup> This was confirmed by measuring the open circuit potential ( $\sim 0.5$  and  $\sim 0.55 V_{\text{RHE}}$ ) in the dark and flat-band potential (0.092 and 0.041  $V_{\text{RHE}}$  (ESI Section 4<sup>†</sup>)) exhibited significant band bending for  $\text{WO}_3/(\text{Ga,W})\text{:BiVO}_4$  and  $\text{WO}_3/\text{S:Bi}_2\text{O}_3/(\text{Ga,W})\text{:BiVO}_4$  photoanodes. From the fs-TA data described above, it is known that a larger number of holes survived the initial electron–hole recombination due to rapid charge separation/transport and subsequent transport to the reactive film surface for the water oxidation reaction.<sup>6,16</sup> Subsequently, from the normalized ns-TA data tracking

secondary decays in Fig. 7c, it was observed that  $\text{WO}_3/\text{S:Bi}_2\text{O}_3/(\text{Ga,W})\text{:BiVO}_4$  exhibited slightly faster ns decay than  $\text{WO}_3/(\text{Ga,W})\text{:BiVO}_4$  but otherwise had nearly identical kinetics. The recorded decay signal was fitted using the exponential decay model. The calculated fitting parameters are summarized in Table S4.<sup>†</sup> The ns-TA best fit with 4 exponentials due to the presence of long-lived carriers. The shortest time scale ( $\tau_1$ ) for  $\text{WO}_3/\text{S:Bi}_2\text{O}_3/(\text{Ga,W})\text{:BiVO}_4$  might represent carrier loss due to the initial, more rapid sweeping of the surface as facilitated by the additional layer. The electron extraction ( $K_{\text{TA}}$ ) rate was higher for the  $\text{WO}_3/\text{S:Bi}_2\text{O}_3/(\text{Ga,W})\text{:BiVO}_4$  photoanode that denoted the enhanced electron mobility after placing the  $\text{S:Bi}_2\text{O}_3$  layer and impact of S diffusion to adjacent layers.

Correspondingly, the recombination between trapped holes and free electrons ( $\tau_2$ ) on the  $>30$  ns timescale was similar in  $\text{WO}_3/\text{S:Bi}_2\text{O}_3/(\text{Ga,W})\text{:BiVO}_4$  (36 ns) compared to that in  $\text{WO}_3/(\text{Ga,W})\text{:BiVO}_4$  (43 ns). The recombination of the trapped hole with thermalized electrons ( $\tau_3$ ) occurred in the  $\mu\text{s}$  range (1.1 to 1.3  $\mu\text{s}$ ) and it was expected that it would not significantly impact the overall water splitting process.<sup>16</sup> By the time the  $\mu\text{s}$  timescale is reached, the leftover carriers surviving recombination have been swept far away from the internal interface, where composition is distinct between the samples, to the

semiconductor/electrolyte interface where composition and thus the kinetics become similar. This study provides evidence that the number of long-lived photogenerated charge carriers is improved after adding the S:Bi<sub>2</sub>O<sub>3</sub> interfacial layer. In addition, we conclude that WO<sub>3</sub>/S:Bi<sub>2</sub>O<sub>3</sub>/(Ga,W):BiVO<sub>4</sub> decays faster in the <10 ns regime compared with WO<sub>3</sub>/(Ga,W):BiVO<sub>4</sub>, suggesting an improved electron transfer rate and accumulation of holes at the (Ga,W):BiVO<sub>4</sub> surface for water oxidation kinetics.

The primary electron and hole separation and transfer pathways occurring among three oxides were shown in the band diagram (Fig. 7d). The CB edge was determined using the flat-band potential considering the negligible difference between the flat-band and bottom of the CB edge.<sup>32</sup> It was assumed that the small amount of S would not significantly change the VB and CB position of Bi<sub>2</sub>O<sub>3</sub>, WO<sub>3</sub> and (Ga,W):BiVO<sub>4</sub> layers. Being the main absorber, BiVO<sub>4</sub> will absorb low energy photons ( $\lambda \leq 530$ ), while WO<sub>3</sub> ( $\lambda \leq 450$ ) and S:Bi<sub>2</sub>O<sub>3</sub> ( $\lambda \leq 430$ ) will absorb high energy photons. Due to the stepped alignment and the appropriate VB and CB configurations, electrons can readily transport from the CBs of BiVO<sub>4</sub> into WO<sub>3</sub> *via* the S:Bi<sub>2</sub>O<sub>3</sub> interfacial layer and into to the current collector.<sup>5,6</sup> Simultaneously, photogenerated holes at WO<sub>3</sub> will transport to and be collected at (Ga,W):BiVO<sub>4</sub> through the S:Bi<sub>2</sub>O<sub>3</sub> interfacial layer.

The time scales for charge separation and transport from TRPL, fs- and ns-TA analysis indicate that more holes are directed to the reactive surface on the ps–ns range in (Ga,W):BiVO<sub>4</sub>. Subsequently, photogenerated electrons will transfer from S:Bi<sub>2</sub>O<sub>3</sub> to WO<sub>3</sub> on a ns– $\mu$ s time scale. Recombination of photoexcited free electrons in (Ga,W):BiVO<sub>4</sub> is reduced by them being transferred into the CB of WO<sub>3</sub> *via* the S:Bi<sub>2</sub>O<sub>3</sub> layer. Once in WO<sub>3</sub>, the electrons have a longer lifetime.<sup>8</sup> In this process, S:Bi<sub>2</sub>O<sub>3</sub> plays a key role in facilitating rapid charge transfer initially to WO<sub>3</sub> to improve the photoactivity of the WO<sub>3</sub>/S:Bi<sub>2</sub>O<sub>3</sub>/(Ga,W):BiVO<sub>4</sub> photoanode. Furthermore, the backflow of charge carriers within the photoanode is reduced by the CB and VB energy barriers present among the WO<sub>3</sub>, S:Bi<sub>2</sub>O<sub>3</sub> and (Ga,W):BiVO<sub>4</sub> layers that suppress hole and electron backflow.<sup>33–35</sup>

As observed from Fig. 8a, the photocurrent density of all photoanodes decreases initially due to dominant photo-corrosion of (Ga,W):BiVO<sub>4</sub> from the loss of V<sup>5+</sup> ions in the form of V<sub>2</sub>O<sub>5</sub>. However, the photocurrent density further ameliorates when V<sub>2</sub>O<sub>5</sub> dissolution gets saturated<sup>36</sup> as can be observed for the WO<sub>3</sub>/(Ga,W):BiVO<sub>4</sub> photoanode, which could retain ~60% of the initial photocurrent density. Further, the effect of the Bi<sub>2</sub>O<sub>3</sub> and S:Bi<sub>2</sub>O<sub>3</sub> interfacial layers becomes more pronounced in ameliorating the charge dynamics and photocatalytic performance of WO<sub>3</sub>/Bi<sub>2</sub>O<sub>3</sub>/(Ga,W):BiVO<sub>4</sub> and WO<sub>3</sub>/S:Bi<sub>2</sub>O<sub>3</sub>/(Ga,W):BiVO<sub>4</sub> photoanodes by retaining ~80 and ~85% of the initial photocurrent density. Consequently, adding a protective layer of Co-Pi demonstrates a self-healing nature and the WO<sub>3</sub>/S:Bi<sub>2</sub>O<sub>3</sub>/(Ga,W):BiVO<sub>4</sub>/Co-Pi photoanode performance improves by retaining 90% of the photocurrent density compared to ~85% for the WO<sub>3</sub>/S:Bi<sub>2</sub>O<sub>3</sub>/(Ga,W):BiVO<sub>4</sub> photoanode after 10 h.<sup>5</sup> The repeatability of the photoanodes after stability measurement demonstrated no significant change in the photocurrent onset and PCD at 1.23 V<sub>RHE</sub> (Fig. S11†). The amount of H<sub>2</sub> and O<sub>2</sub> gases generated was measured to verify the faradaic efficiency of each water splitting half-reaction. The measurement was performed for the WO<sub>3</sub>/S:Bi<sub>2</sub>O<sub>3</sub>/(Ga,W):BiVO<sub>4</sub>/Co-Pi photoanode at 1.23 V<sub>RHE</sub> under simulated AM 1.5G illumination in KPi electrolyte. Fig. 8b shows the H<sub>2</sub> and O<sub>2</sub> gas generation rate (67.3 and 33.6  $\mu\text{mol h}^{-1} \text{cm}^{-2}$ , respectively) along with the theoretical production rate and the corresponding faradaic efficiency (secondary Y-axis in Fig. 8b) values (91.5 and 88%, respectively). The slightly lower values of faradaic efficiency are attributed to the inhibition of proton reduction, diffusion of H<sub>2</sub> gases, and potential back reactions at the counter electrode from dissolved O<sub>2</sub>.<sup>22,23</sup>

Several efforts have been made by our or other groups in the field for improving interfacial passivation, charge transfer and reducing recombination sites by additional (interfacial or under/over) layers in WO<sub>3</sub>/BiVO<sub>4</sub> heterojunction photoanodes. The obtained photocurrent densities at 1.23 V<sub>RHE</sub> are plotted in Fig. 9a and Table S5.† Choi *et al.*<sup>37</sup> incorporated a mild W doped BiVO<sub>4</sub> interfacial layer in the WO<sub>3</sub>/BiVO<sub>4</sub> heterojunction for unidirectional charge flow. Zhang *et al.*<sup>38</sup> designed a three-story

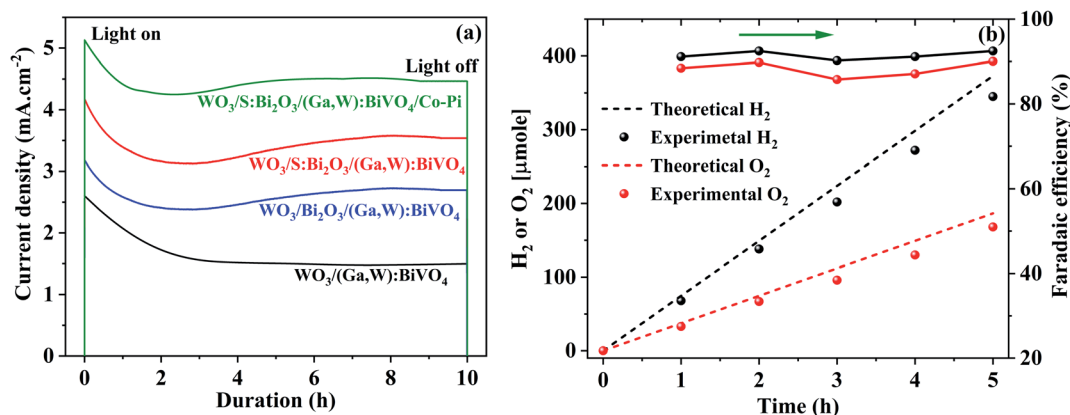


Fig. 8 (a) Photoelectrochemical stability measurements of photoanodes with the WO<sub>3</sub> heterojunction and Bi<sub>2</sub>O<sub>3</sub> interface layer without and with sulfur modification. (b) Evolution of H<sub>2</sub> and O<sub>2</sub> gases from the WO<sub>3</sub>/S:Bi<sub>2</sub>O<sub>3</sub>/(Ga,W):BiVO<sub>4</sub>/Co-Pi photoanode. The measurements were conducted at 1.23 V<sub>RHE</sub> in KPi electrolyte under simulated AM 1.5G illumination.

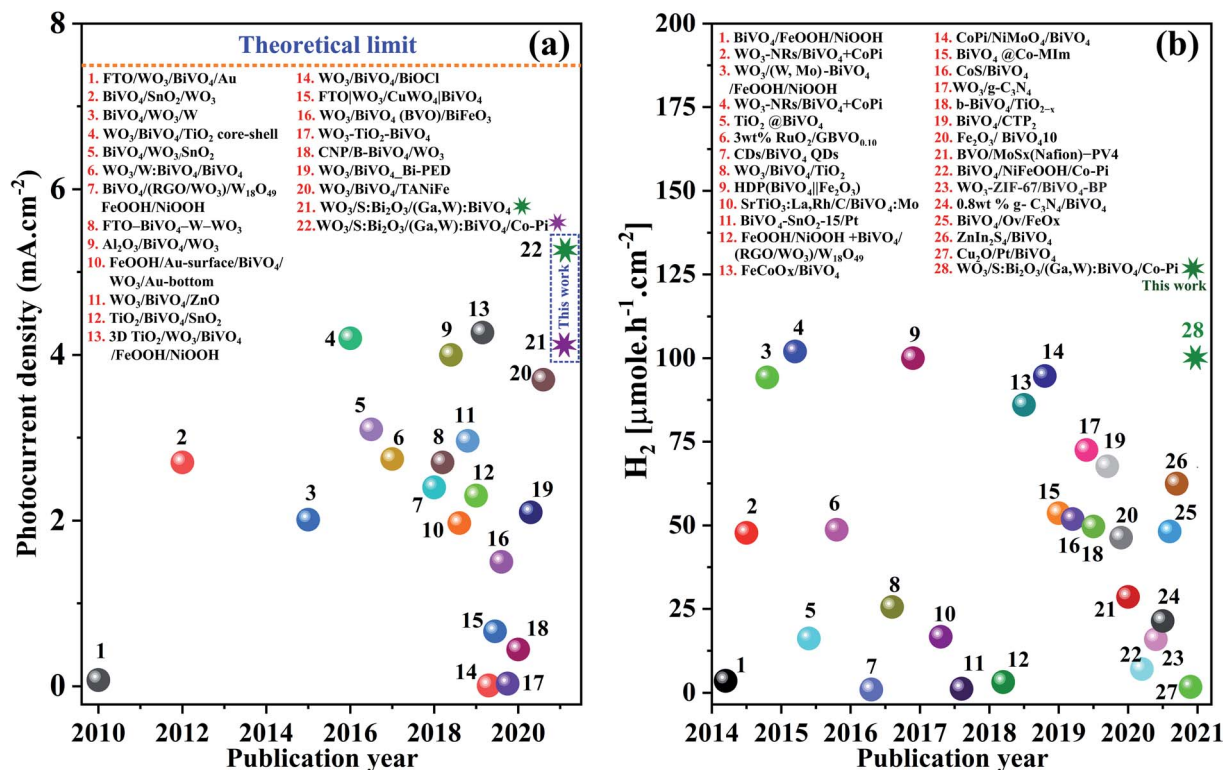


Fig. 9 Comparison of (a) photocurrent density values of  $\text{WO}_3/\text{BiVO}_4$  heterojunction photoanodes with additional (interfacial or under/over) layers, and (b) rate of hydrogen production for  $\text{BiVO}_4$  based heterojunction photoanodes at  $1.23 V_{\text{RHE}}$  under simulated AM 1.5G illumination summarized from the literature (see Table S5 in ESI† file), including this work.

device to improve the conductivity by placing reduced graphene oxide between  $\text{WO}_3$  and  $\text{BiVO}_4$  layers that acted as a multi-channel pathway. A Z-scheme device was designed by Wang *et al.*<sup>39</sup> by incorporating a W-layer between  $\text{BiVO}_4$  and  $\text{WO}_3$  layers for accessing holes. Beak *et al.*<sup>40</sup> used a porous  $\text{SnO}_2$  underlayer in the  $\text{WO}_3/\text{BiVO}_4$  heterojunction where  $\text{WO}_3/(\text{WO}_3 + \text{SnO}_2)$  layers formed a mixed composite for better contact and low resistance. Fig. 9b and Table S6† compare hydrogen production rates at  $1.23 V_{\text{RHE}}$  under simulated AM 1.5G illumination for  $\text{BiVO}_4$  based heterojunction photoanodes along with the present results of our  $\text{WO}_3/\text{S:Bi}_2\text{O}_3/(\text{Ga,W})\text{:BiVO}_4/\text{Co-Pi}$  photoanode. Our results are among the highest reported photocurrent densities and hydrogen production rates.

## 4. Conclusion

The performance of photoanodes containing a  $\text{WO}_3/\text{BiVO}_4$  heterojunction is limited, in part, by charge separation, transfer and recombination across the heterojunction interface. To mitigate these losses, a sulfur modified  $\text{Bi}_2\text{O}_3$  interfacial layer was introduced between  $\text{WO}_3$  and  $\text{BiVO}_4$  layers. The  $\text{BiVO}_4$  layer was optimized with co-doping at  $\text{Bi}^{3+}$  and  $\text{V}^{5+}$  sites with  $\text{Ga}^{3+}$  and  $\text{W}^{6+}$ , respectively, to improve the light absorption and photogenerated charge carrier extraction. The  $\text{S:Bi}_2\text{O}_3$  layer between  $\text{WO}_3$  and  $(\text{Ga,W})\text{:BiVO}_4$  and the Co-Pi co-catalyst led to achieving a photocurrent density of  $5.1 \pm 0.25 \text{ mA cm}^{-2}$  and a hydrogen generation rate of  $67.3 \mu\text{mol h}^{-1} \text{ cm}^{-2}$  for the  $\text{WO}_3/\text{S:Bi}_2\text{O}_3/(\text{Ga,W})\text{:BiVO}_4/\text{Co-Pi}$  photoanode. EDAX, XPS and TOF-SIMS depth profiling

corroborated the uniform diffusion of S in all layers whereas EIS and TRPL confirmed the enhanced interfacial charge transfer kinetics. Subsequently, *operando* fs- and ns-TA analysis concluded that more long-lived photogenerated charge carriers remain after adding the  $\text{S:Bi}_2\text{O}_3$  interfacial layer, providing more holes directed to the reactive surface due to effective charge separation/transfer, and improved the overall photoanode performance. The photocurrent density and hydrogen production rates are among the highest reported for interlayer enhanced  $\text{WO}_3/\text{BiVO}_4$  heterojunction photoanodes.

## Funding

Financial support from Arizona State University is acknowledged. This work was authored in part by the National Renewable Energy Laboratory (NREL), operated by Alliance for Sustainable Energy, LLC, for the U.S. Department of Energy (DOE) under Contract No. DE-AC36-08G028308. The authors acknowledge research support from the HydroGEN Advanced Water Splitting Materials Consortium, established as part of the Energy Materials Network under the U.S. Department of Energy, Office of Energy Efficiency and Renewable Energy, Fuel Cell Technologies Office, under Contract No. DE-AC36-08G028308 to the NREL. J. C. J. acknowledges the Solar Photochemistry Program of the U.S. Department of Energy, Office of Basic Energy Sciences, Division of Chemical Sciences, Biosciences and Geosciences for transient absorption experiments. The views expressed in the article do not necessarily represent the

views of the DOE or the U.S. Government. The U.S. Government and the publisher, by accepting the article for publication, acknowledge that the U.S. Government retains a nonexclusive, paid-up, irrevocable, worldwide license to publish or reproduce the published form of this work, or allow others to do so, for U.S. Government purposes.

## Conflicts of interest

The authors declare no conflicts of interest.

## Acknowledgements

We thank Elisa M. Miller, Andrew Ferguson, Steve Johnston and Jyoti Prakash for valuable discussions and Melissa K. Gish for TA measurements.

## References

- U. Prasad, *ACS Symp. Ser.*, 2020, **1364**, 137–167.
- B. C. Xiao, L. Y. Lin, J. Y. Hong, H. S. Lin and Y. T. Song, *RSC Adv.*, 2017, **7**, 7547–7554.
- T. Li, J. He, B. Peña and C. P. Berlinguette, *Angew. Chem., Int. Ed.*, 2016, **55**, 1769–1772.
- J. Prakash, U. Prasad, R. Alexander, J. Bahadur, K. Dasgupta and A. N. M. Kannan, *Langmuir*, 2019, **35**, 14492–14504.
- U. Prasad, J. Prakash, X. Shi, S. K. Sharma, X. Peng and A. M. Kannan, *ACS Appl. Mater. Interfaces*, 2020, **12**, 52808–52811.
- S. Selim, L. Francàs, M. García-Tecedor, S. Corby, C. Blackman, S. Gimenez, J. R. Durrant and A. Kafizas, *Chem. Sci.*, 2019, **10**, 2643–2652.
- Y. Ma, S. R. Pendlebury, A. Reynal, F. Le Formal and J. R. Durrant, *Chem. Sci.*, 2014, **5**, 2964–2973.
- I. Grigioni, L. Ganzer, F. V. A. Camargo, B. Bozzini, G. Cerullo and E. Selli, *ACS Energy Lett.*, 2019, **4**, 2213–2219.
- I. Grigioni, M. Abdellah, A. Corti, M. V. Dozzi, L. Hammarström and E. Selli, *J. Am. Chem. Soc.*, 2018, **140**, 14042–14045.
- U. Prasad, J. Prakash and A. M. Kannan, *Sustainable Energy Fuels*, 2020, **4**, 1496–1506.
- J. M. Lee, J. H. Baek, T. M. Gill, X. Shi, S. Lee, I. S. Cho, H. S. Jung and X. Zheng, *J. Mater. Chem. A*, 2019, **7**, 9019–9024.
- U. Prasad, J. Prakash, S. K. Gupta, J. Zuniga, Y. Mao, B. Azeredo and A. N. M. Kannan, *ACS Appl. Mater. Interfaces*, 2019, **11**, 19029–19039.
- R. T. Gao, D. He, L. Wu, K. Hu, X. Liu, Y. Su and L. Wang, *Angew. Chem., Int. Ed.*, 2020, **59**, 6213–6218.
- J. Prakash, U. Prasad, X. Shi, X. Peng, B. Azeredo and A. M. Kannan, *J. Power Sources*, 2020, **448**, 227418.
- U. Prasad, J. Prakash, B. Azeredo and A. Kannan, *Electrochim. Acta*, 2019, **299**, 262–272.
- I. Grigioni, K. G. Stampelcoskie, E. Selli and P. V. Kamat, *J. Phys. Chem. C*, 2015, **119**, 20792–20800.
- J. Su, L. Guo, N. Bao and C. A. Grimes, *Nano Lett.*, 2011, **11**, 1928–1933.
- D. Kuciauskas, J. N. Duenow, A. Kanevce, J. V. Li, M. R. Young, P. Dippo and D. H. Levi, in *2012 38th IEEE Photovoltaic Specialists Conference*, 2012, pp. 1721–1726.
- J. L. Young, M. A. Steiner, H. Döscher, R. M. France, J. A. Turner and T. G. Deutsch, *Nat. Energy*, 2017, **2**, 1–8.
- J. Xie, C. Guo and C. M. Li, *Phys. Chem. Chem. Phys.*, 2013, **15**, 15905–15911.
- K. Pal, S. Parmar, J. Kang, A. Bist, P. Dua and S. Jang, *ChemSusChem*, 2012, **5**, 1926–1934.
- Y. Pihosh, I. Turkevych, K. Mawatari, T. Asai, T. Hisatomi, J. Uemura, M. Tosa, K. Shimamura, J. Kubota, K. Domen and T. Kitamori, *Small*, 2014, **10**, 3692–3699.
- X. Shi, I. Y. Choi, K. Zhang, J. Kwon, D. Y. Kim, J. K. Lee, S. H. Oh, J. K. Kim and J. H. Park, *Nat. Commun.*, 2014, **5**, 1–8.
- X. Luo, G. Zhu, J. Peng, X. Wei, M. Hojamberdiev, L. Jin and P. Liu, *Appl. Surf. Sci.*, 2015, **351**, 260–269.
- R. Wang, D. Li, H. Wang, C. Liu and L. Xu, *Nanomaterials*, 2019, **9**, 1341.
- F. Han, H. Li, L. Fu, J. Yang and Z. Liu, *Chem. Phys. Lett.*, 2016, **651**, 183–187.
- M. Lamers, W. Li, M. Favaro, D. E. Starr, D. Friedrich, S. Lardhi, L. Cavallo, M. Harb, R. Van De Krol, L. H. Wong and F. F. Abdi, *Chem. Mater.*, 2018, **30**, 8630–8638.
- B. Klahr, S. Gimenez, F. Fabregat-Santiago, T. Hamann and J. Bisquert, *J. Am. Chem. Soc.*, 2012, **134**, 4294–4302.
- X. Shi, I. Herranz-Cardona, L. Bertoluzzi, P. Lopez-Varo, J. Bisquert, J. H. Park and S. Gimenez, *Phys. Chem. Chem. Phys.*, 2016, **18**, 9255–9261.
- D. Kim, Z. Zhang and K. Yong, *Nanoscale*, 2018, **10**, 20256–20265.
- J. Ravensbergen, F. F. Abdi, J. H. van Santen, R. N. Frese, B. Dam, R. van de Krol and J. T. M. Kennis, *J. Phys. Chem. C*, 2014, **118**, 27793–27800.
- J. Resasco, H. Zhang, N. Kornienko, N. Becknell, H. Lee, J. Guo, A. L. Briseno and P. Yang, *ACS Cent. Sci.*, 2016, **2**, 80–88.
- R. Saito, Y. Miseki and K. Sayama, *Chem. Commun.*, 2012, **48**, 3833–3835.
- M. W. Kim, B. Joshi, E. Samuel, K. Kim, Y. Il Kim, T. G. Kim, M. T. Swihart and S. S. Yoon, *J. Alloys Compd.*, 2018, **764**, 881–889.
- S. Lee, J. Song, Y.-R. Jo, K. S. Choi, J. Lee, S. Seo, T. L. Kim, H. W. Jang, C. Jeon, B.-J. Kim, B. Kim and S. Lee, *ACS Appl. Mater. Interfaces*, 2019, **11**, 44069–44076.
- D. K. Lee and K.-S. Choi, *Nat. Energy*, 2017, **3**, 53–60.
- J. Choi, P. Sudhagar, J. H. Kim, J. Kwon, J. Kim, C. Terashima, A. Fujishima, T. Song and U. Paik, *Phys. Chem. Chem. Phys.*, 2017, **19**, 4648–4655.
- Z. Zhang, B. Chen, M. Baek and K. Yong, *ACS Appl. Mater. Interfaces*, 2018, **10**, 6218–6227.
- R. Wang, T. Xie, T. Zhang, T. Pu, Y. Bu and J. P. Ao, *J. Mater. Chem. A*, 2018, **6**, 12956–12961.
- J. H. Baek, B. J. Kim, G. S. Han, S. W. Hwang, D. R. Kim, I. S. Cho and H. S. Jung, *ACS Appl. Mater. Interfaces*, 2017, **9**, 1479–1487.